Optical and Quantum Electronics (2026) 58:174
https://doi.org/10.1007/s11082-026-08751-1

Multi-mode photonic microchip resonator with response in visible wavelength range: theoretical modelling followed by detailed statistical robustness assessment

Mahdi Khalili Hezarjaribi[1] · Sepehr Razi[2,3] · Fatemeh Ghasemi[4]

Received: 30 September 2025 / Accepted: 2 March 2026

Abstract

A compact photonic micro-cavity chip is introduced for high-precision wavelength control. The chip consists of a fused silica central core placed between two photonic crystal mirrors, with dye-filled spacer layers that actively amplify light for improving spectral sharpness and quality. The platform allows precise tuning of the transmission peaks by adjusting not only the crystal features but also using the core's refractive index profile. For this purpose, three cavity structures, featuring central core layers with uniform, linear, and parabolic refractive index profiles, are designed and analyzed using the characteristic matrix method. Q-factor, finesse, and mode volume were calculated to evaluate resonance quality and provide a basis for design comparison and practical applicability. To address the real-world manufacturing variations, results' reliability were further tested using Monte Carlo simulations. Three key metrics, spectral correlation coefficient (SCC), spectral fidelity index (SFI), and peak position stability (PPS) were analyzed under different tolerance conditions. Results show that while all the proposed cavities have strong potential for the considered aim, the one with a linearly graded refractive index in the defect layer performs the best.

Keywords Photonic cavity · Microchip · Graded index · Resonant mode · Active layer · Statistical assay

✉ Fatemeh Ghasemi
fatemeh.ghasemi@desy.de

1 Institute for Applied Physics, Technische Universität Braunschweig, Brunswick, Germany

2 Leibniz Institute of Photonic Technology, Albert-Einstein-Str. 9, 07745 Jena, Germany

3 Cluster of Excellence Balance of the Microverse, Friedrich Schiller University Jena, 07743 Jena, Germany

4 Deutsches Elektronen-Synchrotron DESY, Notkestraße 85, 22607 Hamburg, Germany

Published online: 17 March 2026

1 Introduction

In many advanced applications such as biophotonics, laser material processing, high-resolution imaging and wavelength-division multiplexing (WDM), it is critically important to excite or detect light at very precise and specific wavelengths (Ghasemi et al. 2019a; Razi et al. 2015; Ghasemi and Razi 2021a; Hu and Chen 2024). In biophotonic imaging or spectroscopy systems, targeting particular wavelengths is essential for fluorescence excitation, molecular absorption, or label-free detection, as sensitivity and specificity rely seriously on a narrow spectral control (Ghasemi et al. 2019a; Razi et al. 2015; Ghasemi and Razi 2021a). On the other side, in WDM, specific wavelengths are crucial because each wavelength carries a separate data in a channel and any wavelength drift or imprecision would cause signal interference and data loss between channels (Hu and Chen 2024). Furthermore, having such wavelength-selection elements is not just convenient but in fact it is essential for enabling high-precision, compact, and tunable systems in next-generation point-of-care devices and integrated lab-on-chip platforms (Mitra et al. 2024; Roshan Entezar et al. 2022). Additionally, similar necessity exists for other applications such as developing advanced cosmological cameras (Hua et al. 2021; Crowther 2022).

However, lasers are not available at all desired wavelengths and nonlinear optical based wavelength conversation methodologies are very complicated and costly (Crowther 2022; Jahangiri et al. 2024). Therefore, optical elements capable of picking specific wavelengths from broadband sources are highly needed. The most common platforms in this regard are multi-resonant filters, photonic crystal cavities, and engineered resonators that act as precise spectral selectors, providing needed wavelengths cost effectively (Jahangiri et al. 2024; Yuan et al. 2025; Xu et al. 2015; Yu et al. 2024; Zhou et al. 2025; Fedoseev and Zhupanov 2021). Photonic crystal microcavities (especially 2D ones) have been extensively studied across various wavelength ranges due to their ability to confine light in small volumes with high quality factors. However, they mostly cover the infrared and mid-infrared regions for telecommunications and sensing applications (Kassa-Baghdouche and Cassan 2019; Serna et al. 2016; Akahane et al. 2005; Nakamura et al. 2016), and there are limited reports on visible-range in comparison (Kassa-Baghdouchea et al. 2015). More recently published papers in the topic can be found in references (Muhammad et al. 2024; Kim et al. 2025; Liu and Long 2025; Plock et al. 2024). Also it is worth noting that for 1D case, items based on the Fabry–Pérot (FP) cavity remain highly popular due to their simplicity, high spectral resolution, and compactness (Zhou et al. 2025; Fedoseev and Zhupanov 2021). While conventional FP resonators naturally produce equally spaced modes, advanced designs allow for arbitrarily spaced resonances by incorporating multiple coupled cavities, structures based on layer thickness variation, or configurations utilizing photonic crystals (Qi et al. 2018; Cao et al. 2024). Given their versatility and performance, this hybrid approach combines Fabry–Perot cavities with photonic crystals to create a powerful platform. It offers sharp wavelength control, enhanced resonance effects, and better mode selectivity provided by PCs with good tunability and integration possibilities delivered by FP cavity. In other words, these unique structures deliver the situation to bypass the band gap condition in transmittance spectrum of the cavity in some specific wavelengths to generate desired resonance modes at wanted ones (Qi et al. 2018; Cao et al. 2024; Wu et al. 2025, 2023; Sepahvandi et al. 2023). Thus by carefully adjusting the PC and FP features, light heating the element will only satisfy the resonance conditions at specific wavelengths which can effectively pass the photonic cavity while the remaining is blocked. One can reach valuable insight in the developed methodologies in this regard at already published papers in references (Qi et al. 2018; Cao et al. 2024; Wu et al. 2025, 2023; Sepahvandi et al. 2023). While emphasizing that each of these previous reports has played a valuable role in this practical field, but it should be noted that most of them are based on complicated platforms including high number of involved layers or complex shapes which can easily make their production very challenging. Furthermore, most published papers in this field only model their multimode cavities under ideal theoretical conditions. However, in practice and during the fabrication process, many factors can deviate from the ideal conditions, and therefore possible tolerances from the perfect parameters should be considered during the modeling process (Wafa et al. 2021).

To meet the existing practical necessities and benefiting proven potential of PC structures in light manipulation applications (Ben Ali 2017; Hu et al. 2018; Wang et al. 2025; Gua et al. 2024), a polychromatic photonic cavity microchip is proposed which includes a micrometer sized fused silica sandwiched between two precisely designed PC mirrors. Furthermore, extra two spacers are placed in between the central core and the mirrors at each side which can be filled with either passive air or active materials. In other words, in the suggested structure despite the other common PC based filters (Gua et al. 2024; Razi and Ghasemi 2019a; Alrowaili et al. 2023), a focus has been considered on having active layers of dyes in the body of the element. These layers provide optical gain that compensates losses in the photonic crystal structure, resulting in enhanced resonant mode intensities and improved filter performances with sharper spectral features and higher quality factors. All these features can provide more robust and effective properties for high precision wavelength selection applications.

This work introduces multiple novelties in the design and analysis of photonic crystal microresonators. Unlike previous reports discussed above that consider very complicated structures made of layers mostly with uniform structures, here we study in detail very simple structure but evaluating how engineered index gradients (uniform, linear, and parabolic profiles) in the central cavity layer can significantly influence optical performance. Additionally, the effect of the presence of an active layer (Rh6G dye) in the body of the crystal has been considered. Focusing on the visible range is another advantage of this study, which has been discussed very limitedly as mentioned before. We selected one-dimensional photonic crystals due to their practical advantages: ease of fabrication using standard deposition techniques, cost-effectiveness, straightforward integration into planar optical systems, and computational efficiency in modeling. The proposed structures feature simple arrangements using common photonic materials, making them practically viable. Furthermore, we employ Monte Carlo statistical analysis to evaluate the robustness of these structures against fabrication imperfections, which is crucial for assessing real-world device performance.

Structural details of the proposed photonic cavities as well as the physical rules and mathematical methods that have been considered in the modeling of the optical responses are discussed first in the following. Then, the optical features of the cavities and the tunability of their characteristics using internal and external parameters are discussed comprehensively and the physical phenomena playing a role in the results are explained. Next, a detailed statistical analysis of how fabrication errors may affect the cavities' optical properties is performed. Finally in summary the advantages of the suggested platform and its potential for applications requiring precise wavelength control are concluded.

2 Material and mathematical methods

2.1 Micro-cavity structure

The configurations of the proposed photonic micro-cavities are depicted schematically in Fig. 1. Panel (a) illustrates the architecture comprising two photonic crystals (PCs) with TiO_2/SiO_2 unit cells in a mirror-symmetric arrangement enclosing a micrometer-scaled SiO_2 layer exhibiting a uniform refractive index profile. A spacer layers which could be filled by either air or an active material such as Rhodamine 6G (Rh6G) are positioned between each PC and the central layer. Thus the cavity follows the pattern: $[TiO_2/SiO_2]^N$/cladding/SiO_2-centralcore/cladding/ $[SiO_2/TiO_2]^N$ where, N denotes the number of the unit cells. Horizontal lines illustrate the refractive index variations in each configuration. The layer thicknesses used in the modeling are 55 nm for TiO_2, 60 nm for SiO_2, and 20 nm for the cladding layer. Also, the corresponding refractive indices are considered as 2.6406 + 0i for TiO_2, 1.4620 + 0i for SiO_2, and 1.7735–0.001i for the Rh6G.

Panels (b-c) represent analogous structures wherein the central core layer of SiO_2 exhibit spatially varying refractive index profiles, linear and parabolic, respectively. More specifically, the refractive index distribution within the central core layer (CCL) of these cavities demonstrates a gradient that changes either linearly or parabolically between the refractive index values of the TiO_2 and SiO_2 constituents in the adjacent PCs. In the following, these architectures are called as uniform index gradient-photonic micro cavity (UIG-PMC), linear index gradient-photonic micro cavity (LIG-PMC), and parabolic index gradient-photonic micro cavity (PIG-PMC). It is also worth noting that the successful deposition of TiO_2 layers on SiO_2 slabs has been already realized experimentally using various technologies

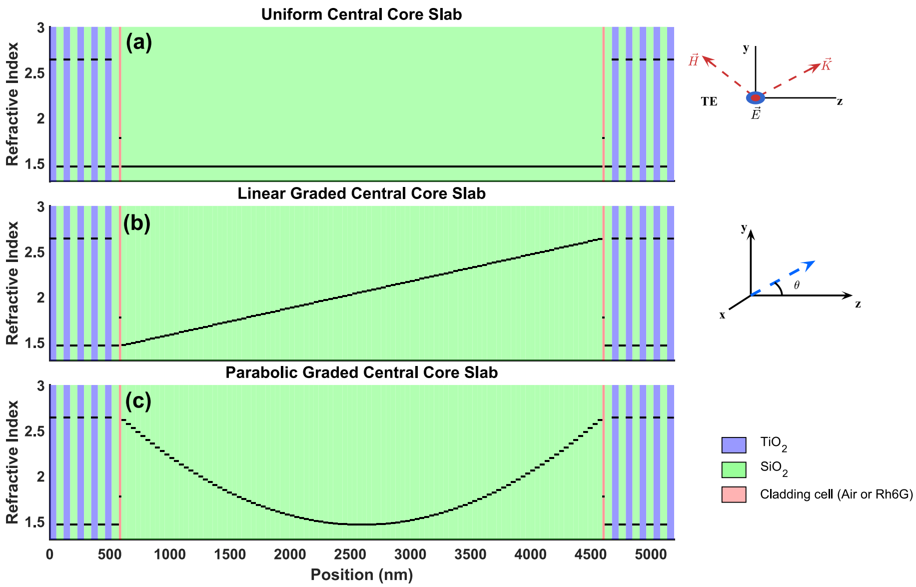

Fig. 1 schematic sketch of the proposed multi-mode photonic cavities made of TiO_2/SiO_2 unit cells and including two cladding layers sandwiching a central defect slab with uniform (upper row), linear (middle row) and parabolic (lower row) refractive index profile. Horizontal lines illustrate the refractive index changes in different layers

(Acosta-Silva et al. 2023; Kim et al. 2006). Furthermore, it has been well proven before that it is possible to construct a smooth gradient across the full thickness by depositing multiple sublayers, each slightly doped to achieve incremental refractive index changes (Kim et al. 2006; Kakiuchida et al. 2007). Also, precise refractive index tuning is possible through controlled doping with oxide materials (Kakiuchida et al. 2007; Li et al. 2002). Thus, almost no serious challenge should exist in fabrication of the suggested structures in practice.

2.2 Mathematical modelling

To extract and analyse the properties of an optical element made of multilayer films, solving Maxwell's equations (MEs) is fundamental (Ghasemi et al. 2021). However, as an alternative to directly solving MEs, one of the most widely used and analytically traceable approaches is the transfer matrix method (TMM) (Razi and Ghasemi 2019b; Segovia-Chaves and Vinck-Posada 2018). This method balances analytical clarity with numerical stability. Its strength lies in handling arbitrary stacks of layers with different refractive indices and thicknesses. It also maintains computational efficiency by taking into consideration of many important physical phenomena such as both transmission and reflections from interfaces or polarization state of the incident electromagnetic wave (Segovia-Chaves and Vinck-Posada 2018; Ghasemi and Razi 2021b). In other words, TMM calculates the optical characteristics by solving Maxwell's equations through boundary conditions at each interface, enabling direct evaluation of reflection and transmission spectra without requiring spatial discretization or meshing, as used in numerical methods such as FDTD or FEM. The key equations involved in this method are: Faraday's and Ampere's laws which are presented in Eqs. 1, 2 respectively for the case there is no free current (Ghasemi et al. 2021; Razi and Ghasemi 2019b).

$$\nabla \times \mathrm{E} = j\omega\mu H \tag{1}$$

$$\nabla \times \mathrm{H} = -j\omega\varepsilon E \tag{2}$$

Under the assumption of having planar media as in our case, these equations reduce to wave equations for the involved electric and magnetic fields. Then it is possible to track how electromagnetic waves behave as they pass through each layer and interface, considering both reflection and transmission. It is worth noting that TMM takes into consideration that each layer of the stack supports forward and backward waves inside. Also it is based on enforcing the continuity of the tangential components of the electric and magnetic fields at the interfaces between adjacent layers. By applying these continuity conditions at every interface and linking them through matrices, TMM builds a complete picture of how the wave behaves across the entire structure. For this purpose, an individual 2×2 matrix is allocated to each layer, incorporating Fresnel reflection and transmission coefficients due to refractive index mismatch at the interfaces, Eq. 3. Here in this equation both the associating dynamical and propagation matrices have been considered. Finally, transfer matrix links the fields at the beginning and end of the stack via multiplying all matrices, Eq. 4. Once the total transfer matrix is known, one can easily extract the transmittance by computing the ratio of transmitted to incident power, using Eq. 5 for TE polarization of the incident light (Segovia-Chaves and Vinck-Posada 2018; Ghasemi and Razi 2021b; Ghasemi et al. 2019b).

$$M_i = \begin{pmatrix} \cos(k_{iz}d_i) & -\frac{j}{p_i}\sin(k_{iz}d_i) \\ -jp_i\sin(k_{iz}d_i) & \cos(k_{iz}d_i) \end{pmatrix} \tag{3}$$

$$M_{total} = (M_{TiO_2}M_{SiO_2})^5 M_{Clad}M_{Core}M_{Clad}(M_{SiO_2}M_{TiO_2})^5 = \begin{pmatrix} m_{11} & m_{12} \\ m_{21} & m_{22} \end{pmatrix} \tag{4}$$

$$\mathrm{T} = 1 - \mathrm{R} - \mathrm{Absorbance}, R = \left| \frac{(m_{11} + m_{12}p_{n+1})p_0 - m_{21} - m_{22}p_{n+1}}{(m_{11} + m_{12}p_{n+1})p_0 + m_{21} + m_{22}p_{n+1}} \right|^2 \tag{5}$$

where, $p_i = k_{iz}/\omega\mu_0$, $p_0 = (\sqrt{\mu_0/\varepsilon_0})\cos(\theta_0)$, $p_{n+1} = (\sqrt{\mu_{n+1}/\varepsilon_{n+1}})\cos(\theta_{n+1})$, ε_0 and ε_{n+1} are denoting the relative dielectric constants of the input and output planes. Furthermore, $k_{iz} = \sqrt{k_0^2\varepsilon_i - k_x^2}$ in which $k_x = k_0 sin\theta_0$. In these equations, i, denotes the layers involved in the cavity structure. During the mathematical modelling, interfaces of the layers are considered parallel to the x–y plane, and the z-axis is assumed to be normal to the surface of the layers of the structure. The surrounding atmosphere is air, and the light incident angle, θ, is measured with respect to the z-axis (Fig. 1).

To assess the quality and practical utility of the generated resonant modes, finesse, Q-factor and mode volume are extracted as performance metrics. These three important parameters measure how sharp, confined and well-defined the resonant peaks are, while higher values in Q-factor and finesse mean less energy is lost and low mode length reflects better spatial condensation of energy inside the resonator leading to more efficient and precise optical performance. These metrics are mathematically defined in Eqs. 6–8 for Q-factor, finesse and modal length respectively (Ben Ali 2017; Bouazzi and Kanzari 2012; Tavakoli and Jalili 2014).

$$\text{Q-Factor} = \frac{\lambda Resonance}{\Delta\lambda} \tag{6}$$

where Δλ is the full width at half maximum (FWHM) and$\lambda_{\mathrm{Resonance}}$ is wavelength of the resonance mode.

$$\text{Finesse} = \frac{\Delta\lambda}{\Delta\lambda} \tag{7}$$

here $\Delta\lambda$ is the wavelength spacing between two adjacent resonant modes. In strong similarity with 3D resonators (Akahane et al. 2005; Ghasemi and Razi 2021b), the mode volume (which is technically called mode length in 1D) can be defined as Eq. 8 where E(z) is the electric field and $\varepsilon\,(z) = \varepsilon_0 n^2(z)$, with ε_0 being the vacuum permittivity (Akahane et al. 2005; Aurelio and Liscidini 2017).

$$L_{mod} = \frac{1}{\max\{\varepsilon(z)|E(z)|^2\}} \int \varepsilon(z)|E(z)|^2 dz \tag{8}$$

It should be noted that for 1D photonic crystal cavities, the normalized confinement length serves as the dimensionally appropriate equivalent of mode volume used in 3D cavity structures. While mode volume quantifies field confinement across all three spatial dimensions, in 1D system where the structure varies only along the stacking direction, the confinement length along this axis becomes the relevant figure of merit for characterizing spatial localization of the resonant modes. To extract the wavelength distribution and energy profile inside the resonator, we have followed the methodology detailed in Aurelio and Liscidini (2017), where readers may consider for further technical information.

2.3 Statistical assessment

In practice, manufacturing tolerances, material inconsistencies, and process variations create unavoidable discrepancies between theoretical models and fabricated elements. The significance of this fact warrants further detailed studies after theoretical modelling. To quantify these effects and ensure robustness of the extracted features, comprehensive statistical analyses are also conducted in our study. In more detail, we selected three critical metrics: spectral correlation coefficient (SCC), spectral fidelity index (SFI), and peak position stability (PPS), defined in Eqs. 9–11 respectively. In statistical spectral analysis, SCC, SFI, and PPS provide complementary perspectives that together offer a comprehensive assessment of spectral quality. While SCC captures the preservation of overall spectral shape through correlation analysis, SFI quantifies intensity fidelity, and PPS evaluates peak positional consistency. These metrics are inherently complementary because sometimes peaks are in the right positions as standard cavity predicts but with wrong heights, and sometimes peaks have right heights but at drifted positions. By employing all three metrics simultaneously, one can distinguish between different types of spectral degradation and obtain more reliable statistical conclusions about system performance and the robustness of the suggested cavities against manufacturing variations. Then we can identify confidence intervals for expected performance beyond ideal theoretical cases.

$$SCC = \frac{\sum_{i=1}^{N}\left(T_{ref}(i) - \overline{T}_{ref}\right)\left(T_{tol}(i) - \overline{T}_{tol}\right)}{\sqrt{\left(\sum_{i=1}^{N}\left(T_{ref}(i) - \overline{T}_{ref}\right)\right)^2\left(\sum_{i=1}^{N}\left(T_{tol}(i) - \overline{T}_{tol}\right)\right)^2}} \tag{9}$$

$$SFI = 1 - \frac{\sum_{i=1}^{N}\left(T_{ref}(i) - T_{tol}(i)\right)}{\sum_{i=1}^{N}\left(T_{ref}(i)\right)} \tag{10}$$

$$PPS = \frac{1}{N_R}\sum_{j=1}^{N_R} max\left\{0, 1 - \frac{max(0, \delta_j - \delta_p)}{\Delta_{max} - \delta_p}\right\} - P_{count}, P_{count} = \alpha\frac{|N_T - N_R|}{N_R} \tag{11}$$

where $T_{ref}(i)$ and $T_{tol}(i)$ are the transmittance values at wavelength point i for the reference (0% tolerance) and tolerance-affected spectra, respectively. $\overline{T}_{ref}$ and $\overline{T}_{tol}$ are the respective mean transmittance values, and N is the number of spectral points. N_T and N_R are number of tolerance-affected peaks and number of the reference peaks respectively and α is asymmetric penalty coefficient. Furthermore, N_R is the number of reference peaks, δj is the wavelength shift of the j-th reference peak to its nearest tolerance peak, δ_p is the perfect zone threshold (accounting for numerical precision) and Δ_{max} is the maximum matching radius.

These metrics are systematically evaluated across various tolerance conditions using Monte Carlo simulations.

3 Results and discussions

3.1 Optical characteristics and parameter dependencies

At the first step, the optical characteristics of the proposed photonic cavity structures were evaluated through transmittance spectra analysis under two distinct conditions. The solid lines in Fig. 2 represent the results for a cavity including cladding layers but not any other defect layer, while the dashed lines demonstrate the case in which the cladding cell is divided into two parts by insertion of a 30 nm thick SiO_2 defect layer with uniform refractive index. Panel (a) illustrates the cavity's response when the cladding layers contain air (a) and panel (b) is for the case in which those layers are filled by Rh6G. Both cases show similar transmittance patterns and roughly same band gap regions, but with notable differences in peak positions. Band gaps (areas of zero transmittance) are evident in both configurations roughly between 400 and 600 nm.

In case there is no central SiO_2 defect layer and when the cladding layers are filled by air, the narrow and sharply defined resonant peak is at 458.3 nm. However, for the case of Rh6G filled one, it appears at 505.7 nm. Insertion of the SiO_2 central layer results in a shift for resonant peaks (~40 nm in the case of air and ~30 nm for Rh6G), while negligible effect for the bandgap. Also it is worth noting that in all cases the intensity amount of the peak for the crystal including Rh6G is more than the case in which cladding layers are filled by air. Transmittance values of more than 1.0 clearly reflect the expected gain effect of the considered dye. I.e. the gain compensates for losses and can lead to amplification, particularly near the resonance wavelengths of the cavity. This amplification has been also documented in previous studies as well (Yi and Li 2021; Zaky et al. 2022). However, the wavelength shift can be attributed to refractive index (RI) changes. I.e. since Rh6G has a higher RI than air,

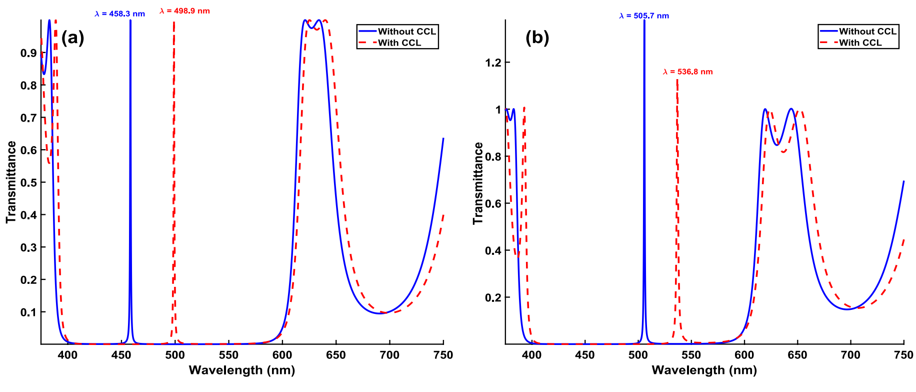

Fig. 2 Transmittance spectra of the suggested cavities in case cladding layers are filled by (**a**) air and (**b**) Rh6G. Solid lines show the spectra of the cavity without any central core layer (CCL), while dashed lines represent optical response when a 30 nm thick SiO_2 slab with uniform refractive index is inserted between the cladding cells (with CCL). Other parameters: unit cell number at each side of the CCL = 5, θ = 0°, polarization: TE

the effective optical path length increases, which results in a redshift of the modes to satisfy the resonant condition (Ghasemi and Razi 2021b; Ghasemi et al. 2019b).

Figure 3 illustrates how the number of the active modes in the cavity depends on the structural parameters and the light incident angle. By active modes, we refer to the resonant modes that appear within the photonic bandgap (PBG) region of the transmission spectrum. These are the cavity modes that are supported by the microresonator structure and exhibit strong resonance characteristics. The upper panels demonstrate the influence of the unit cell quantity and the incident light angle at fixed layer thicknesses.

The lower panels reveal how the dimensional properties of these building blocks within each unit cell affect the mode distribution. This analysis provides valuable design guidance for tailoring photonic cavities to achieve specific modal characteristics for targeted optical application. Results show that for all proposed designs, the number of active modes decreases sharply beyond ~20° incidence angle. However, graded structures sustain pointedly more modes across the 0–20° angular range compared to the uniform case, which achieves a maximum of only 11 modes. Among the designs, the LIG-PMC structure demonstrates superior performance by supporting the highest number of active modes.

The number of active modes also increases with the number of unit cells. The dependency is largely the same in all cases with very small fluctuations in the mode number. However, it saturates around 4 unit-cells in the case of LIG-PMC and PIG-PMC, beyond which no substantial improvement is observed. While for UIG-PMC the maximum is observed above 6 unit-cells. This trend highlights that increasing the number of unit cells enhances mode number, but only up to a limit. The bottom row in Fig. 3 illustrates the influence of TiO_2 and SiO_2 layer thicknesses. For all structures, the number of active modes increases gradually with the layer thicknesses in the range of 20–100 nm, reaching optimal performance when both layers are simultaneously thickened. Afterwards the number of modes decreases with further increase in the layers size. The dependency appears slightly stronger

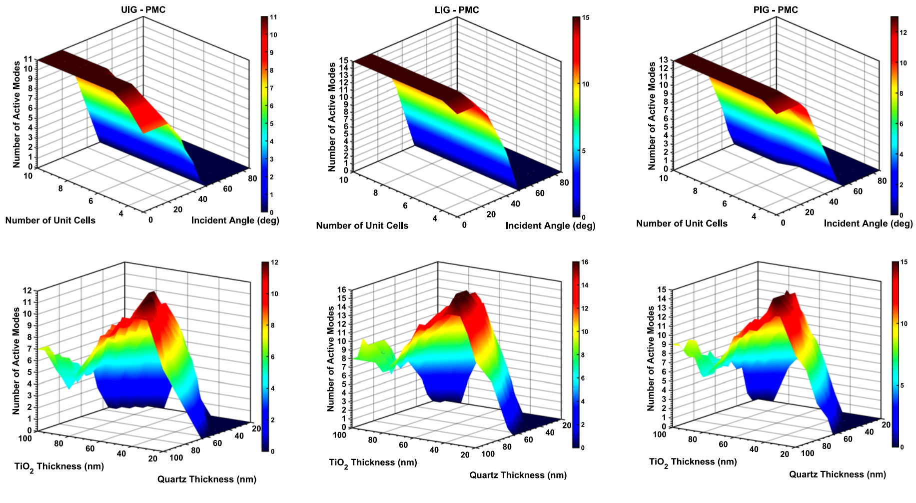

Fig. 3 Dependency of the number of the active modes to the physical features of the cavities. Upper row presents the effect of the number of unit cells and the light incident angle when the thicknesses of the TiO_2 and SiO_2 layers are fixed at 55 and 60 nm respectively. The lower row is the dependency on the thickness of the building blocks of the unit cell while the other parameters are: N = 5, θ = 0°, polarization = TE. CCL thickness = 4 µm

on SiO_2 thickness, indicating its more dominant role in mode enhancement. I.e. the number of active modes changes more dramatically along the SiO_2 axis than the TiO_2 one and small changes in SiO_2 thickness may result in steep increases or decreases in the number of active modes. In contrast, the variation along the TiO_2 thickness axis is more gradual and less steep in overall. The UIG-PMC displays irregular fluctuations, with minimum number of modes but the graded structures are having greater modal capacity. LIG-PMC supports the largest active modes (up to 16), with PIG-PMC following closely, both showing wide, stable regions of optimal thickness combinations. In more detail, peaking range for structure with uniform defect is observed in the interval of 30–60 nm and 40–100 nm for TiO_2 and SiO_2 respectively. While the optimum thickness ranges to have maximum mode numbers in the case of LIG-PMC and PIG-PMC are respectively 25–65 nm and 25–60 nm for TiO_2 layer. This range for SiO_2 layer is between 35–100 and 40–100 for those structures respectively.

At the next step, the influence of the thickness and refractive index profile of the central core layer on the optical response of the suggested photonic cavities were systematically investigated. Figures 4 and 5 present a comprehensive comparison of the optical responses for cavities incorporating central layers with uniform, linear, and parabolic refractive index distributions. Figure 4 demonstrates how defect layer dimension directly impact the number of the resonant modes (a) and the inter-mode spectral spacing (b). Results show increasing the size of the central layer from several tens of nanometre (which was the case in Fig. 3) to micron scale, cause creation of extra modes in the gap region. I.e. as central defect layer thickness increases from 0 to 8000 nm, the number of active modes also increases almost linearly for all three cases. Although the number of modes in three cases are close together at smaller thickness values (<3 μm) but with further increasing the size of the layer, the LIG-PMC rises the fastest, exceeding 30 active modes, while the PIG-PMC case reaches a few less modes at the maximum considered thickness of 8 μm. However, the UIG-PMC case stays much lower with maximum of ~20 modes.

For all three structures an inverse relationship with thickness of the CCL is observed for the average inter-mode spacing. I.e. at small central layer thicknesses and at all three configurations high mode spacing values are observed. But as the thickness increases, average mode spacing drops exponentially in all cases. However, although the curves remain close to each other, the decrease steep for UIG-PMC is the minimum while for the LIG-PMC is maximum and PIG-PMC places in between. This behavior sounds normal as LIG-PMC has the highest number of modes. This suggests that the structure with linearly graded central layer

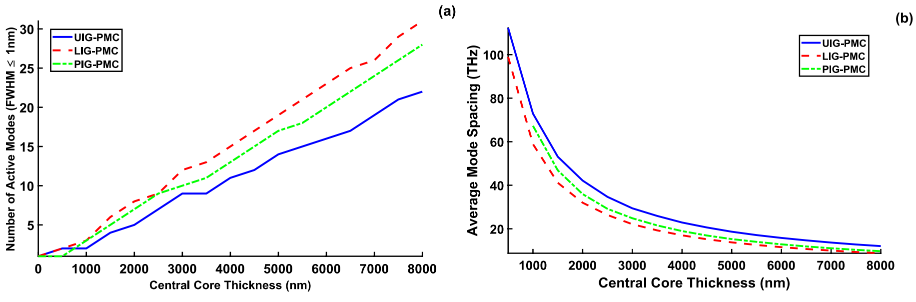

Fig. 4 Effect of the defect layer size on (**a**) the number of active modes and (**b**) the average distance between modes, for the three suggested structures. TiO_2 and SiO_2 layer thicknesses are 55 and 60 nm respectively. Other parameters are considered as: N = 5, θ = 0°, polarization = TE

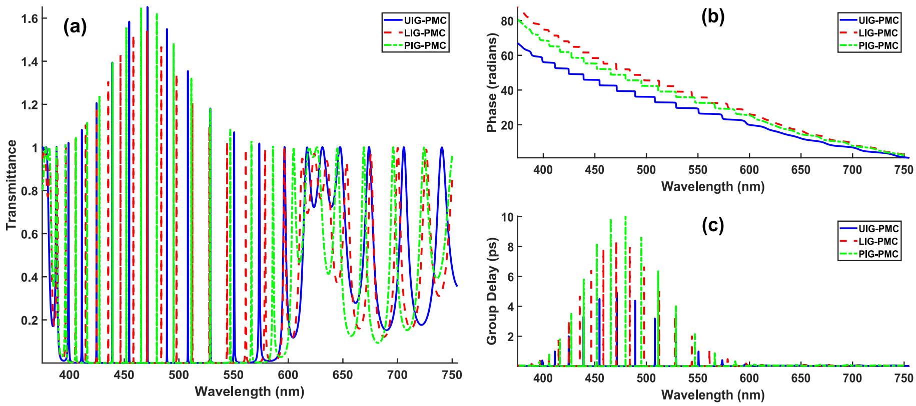

Fig. 5 Comparison of the optical responses of the photonic cavities with central defects having uniform, linear, and parabolic refractive index profiles: **a** transmittance, **b** phase response, and **c** group delay in the visible wavelength range. Other parameters are considered as explained in Fig. 4 and CCL thickness is 4 µm

design (LIG-PMC) allows for more closely packed resonant modes at the same defect thickness compared to the other structures. The observed increase in the number of resonant modes with greater central layer thickness is consistent with the physics of optical cavities and wave localization. A thicker defect layer increases the optical path length, allowing more standing wave conditions to be satisfied within the photonic band gap. This leads to the formation of additional localized resonant modes, each appearing as a distinct transmission peak. The effect is analogous to a Fabry–Pérot resonator, where a larger cavity supports more resonances.

To dive more in depth of the effect of the characteristics of the central core layer on the optical features of the suggested photonic micro cavities, further systematic evaluations are conducted. For this purpose, the transmittance spectra (5a), phase response characteristics (5b), and resulting group delay measurements (5c) across the visible wavelength range are presented in Fig. 5. These comparative results demonstrate how adapting the spatial distribution of the refractive index within the central core layer can effectively modulate key optical properties, providing valuable insights for engineering photonic devices with customized spectral behaviors. These results also clearly confirm that changing the refractive index profile of the central layer from uniform to graded form, cause not only a remarkable shift in the already existing resonant modes but also may increase number of them. The appearance of these distinct resonant modes in the transmittance spectrum, correspond directly to phase discontinuities (steps) in the phase response and pronounced maxima in the group delay spectra at identical wavelengths. In other words, whenever a resonant peak appears in the transmittance spectrum, there is a corresponding step change in the phase response and a spike in the group delay at precisely the same wavelength. These signatures confirm the resonant nature of these modes as expected in micro cavities, making these structures promising candidates for active micro cavity applications.

3.2 Quality analysis of the resonant modes

To provide a more quantitative assessment of the cavity performance, we analysed key metrics characterizing the modes generated in the transmittance spectra of the cavities with

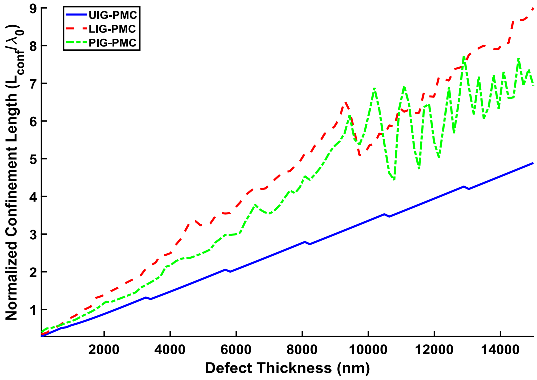

Fig. 6 Normalized confinement length as a function of defect layer thickness for different refractive index profiles. Other parameters are considered as explained in Fig. 4

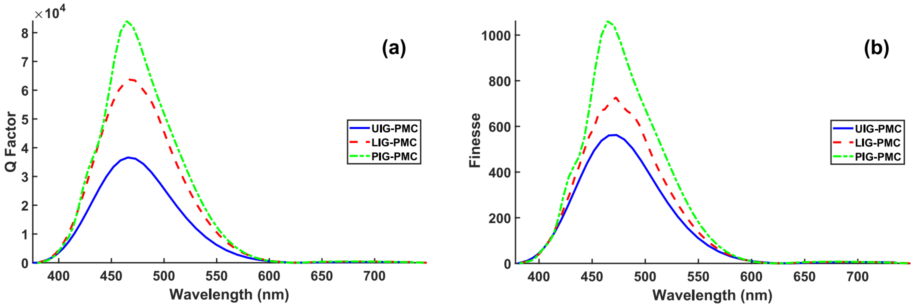

Fig. 7 metrics of the cavity modes generated in transmittance spectra of the cavities including different types of defects in their structure. **a** Quality factor and **b** Finesse of the generated modes. Other parameters are considered as explained in Fig. 4 and CCL thickness is 10 µm

various central core types. Figure 6 illustrates the trade-off between field confinement and cavity thickness through the normalized mode length as a function of defect layer thickness. The uniform profile (UIG-PMC) shows monotonic linear growth. In contrast, both graded-index profiles (LIG-PMC and PIG-PMC) display oscillatory behavior with local minima and maxima at higher thicknesses. These up and downs are offering opportunities to optimize performance at specific thickness values. This is the flexibility not available in conventional uniform-index designs. It is also worth noting that at thickness values more than 10 µm oscillatory fluctuation in mode length gets more significant in graded-index profiles. Thus this value may represent an upper limit for liable cavity performance.

Figure 7 presents this comparative evaluation through two other critical parameters: Quality factor (a) and Finesse (b) of the generated modes. Results show that the quality factor (Q-Factor) rises with wavelength, peaking between 450 and 500 nm for all three cases, before decreasing. The PIG-PMC structure reaches the highest Q-Factor, topping above 85,000, the LIG-PMC cavity peaks around 63,000, and the UIG-PMC peaks just above 38,000. This shows that the PIG-PMC design achieves the best Q-factor, followed by LIG-PMC, while the case with a central layer having a uniform refractive index has the lowest amount across the considered wavelength range. On the other side, similarly, finesse increases with wavelength, peaking between 450 and 500 nm for all three cases before dropping off again. In consistency with what is observed in the Q-Factor studies, the structure with parabolic central layer achieves the highest Finesse value, peaking above 1000, while the LIG-PMC and UIG-PMC cases peak lower, around ~ 760 and ~ 580 respectively. This indicates that the PIG-PMC design offers the best performance also in terms of finesse while roughly close values are observed for the cases of LIG-PMC and UIG-PMC.However, it is important to put light on the fact that, excluding several resonant modes in the mentioned wavelength region that exhibit significantly higher Q-factor differences, the majority of modes in both the PIG-PMC and LIG-PMC structures demonstrate large Q-factor value overlap across the remainder of the spectrum. It is also the case for finesse metric. Thus, it could be concluded that across most of the wavelength range being studied (except for a few specific cases) the two structures have comparable performance characteristics.

Also it is important to pay attention that although several reports describe photonic structures with higher Q-factors or finesse values (Ben Ali 2017; Bouazzi and Kanzari 2012), our structures offer significant practical advantages. For example, the structure in those papers requires an incident angle of ~ 1.5 rad to achieve maximum Q-factor, while their suggested cavity design incorporates several tens of layers, making fabrication extremely challenging from a practical standpoint. Similarly, they recommend hybrid structures combining periodic and Fibonacci or Rudin-Shapiro arrangements to achieve high finesse or Q-factor values. In comparison, our structure is much more practical to implement. It features a simple design with a limited number of layers and uses readily available, well-characterized materials. Most importantly, it operates at 0–20° incidence angle rather than requiring specific, difficult-to-achieve working angles.

Also, there are reports on point-defect 2D/3D photonic cavities with much higher values of Q-factor or finesse (Akahane et al. 2005; Nakamura et al. 2016; Kassa-Baghdouchea et al. 2015; Muhammad et al. 2024; Kim et al. 2025; Liu and Long 2025; Lu et al. 2021). Nonetheless, here it is very necessary to point out that direct comparison of those structures with the suggested ones in this paper is not straightforward due to fundamental differences in confinement mechanisms and dimensionality. But our results show that even though those cases are reaching higher quality values than ours, but we offer acceptable values of critical qualification factors together with advantages in terms of fabrication simplicity and design flexibility. Point-defect cavities typically achieve higher quality factors through complete 3D bandgap confinement but require more complex nano/micro fabrication procedures. The other important point is the performance wavelength. Most of these high quality reports are for IR or MIR range and not for visible interval which is the case in our study. However, there are reports on these structures in the visible spectral range in which the reported Q-factors are lower than those obtained in this work (Kassa-Baghdouchea et al. 2015). Thus, our 1D approach provides a viable alternative for applications where moderate Q-factors combined with ease of implementation are prioritized.

3.3 Statistical analysis of the fabrication tolerance effects

To quantitatively assess the practical feasibility of achieving the theoretical results discussed above, we must consider potential manufacturing mismatches. Therefore, a comprehensive spectral stability analysis is conducted for the suggested structures under varying tolerance conditions. Figure 8 (first row) presents these results through transmittance spectra with 0–10% refractive index variations in TiO_2 and SiO_2 layers. For UIG-PMC, transmittance peaks remain sharp with high intensity up to 2% tolerance, but degrade significantly at higher tolerances. I.e. as the tolerance in the refractive indices of the layers increases, further spectral broadening and reduced peak heights are observed. Almost the same degradation across the spectrum is visible for both LIG-PMC and PIG-PMC structures. But, at these cavities, slightly stronger spectral intensities are observed at 2–5% of tolerance. In all the suggested cavities, increasing the tolerance value over 5% results in moderate spectral smoothing and distortions so that for the peaks between 410 and 550 nm, transmittance values of≤20% is observed. To investigate this dependency quantitatively, Fig. 8 (second row) shows how measurable spectral metrics (SCC, SFI, PPS) change when unit cell layers have refractive index tolerances compared to the ideal case. Results show SCC and PPS remain high and stable across all tolerances for all defect types, but SFI, drops sharply with increasing tolerance. In other words, although spectral correlation coefficient and peak position stability (SCC, PPS) remain largely unaffected, but in all three structures SFI is highly sensitive to the tolerance value in refractive index of the layers. In these results, there is no significant difference between the proposed cavities in agreement with what is observed in the transmission spectra of different structures.

To examine tolerance effects more thoroughly, an extra comparative study is conducted under three conditions: 10% tolerance applied to refractive index of layers only (Δn), their thickness values only (Δd), or both parameters together (Δn+Δd). Results of this analy-

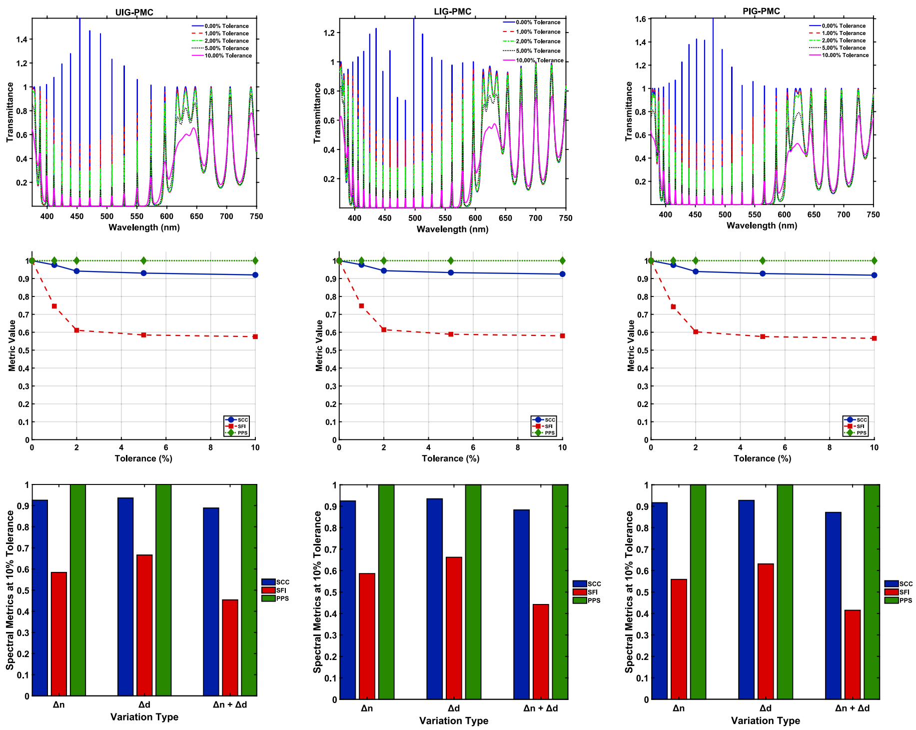

Fig. 8 Spectral stability analysis of three photonic cavities under different tolerance conditions: (First row) Transmittance spectra with 0–10% tolerance in refractive index of TiO_2 and SiO_2 layers, (Middle row) Spectral stability metrics versus tolerance in refractive index, (Lower row) Comparison of stability metrics at 10% tolerance in refractive index only, thickness only, or both parameters combined. Other parameters are considered as explained in Fig. 4 and CCL thickness is 4 µm

sis which are presented in a bar chart format, provides crucial insights into each design's robustness against fabrication variations. Results show that the overall dependency of all three proposed photonic cavities on the considered tolerance effects is qualitatively similar. Also, it is evident that between the evaluated parameters, PPS remains highly stable across all variation types, maintaining values close to 1, indicating strong robustness. In contrast, SFI is the most sensitive metric, showing significant degradation, especially under combined variation (Δn + Δd), where it drops to its minimum value in all three photonic cavities. However, SCC lies in between, showing moderate sensitivity. Furthermore, it is worth noting that tolerance in refractive index of the layers (Δn) induces variations that lead to greater performance degradation than Δd alone. This indicates that refractive index fluctuations have a more pronounced effect on the spectral stability of the cavities than the potential tolerances in layer thickness.

To identify which configuration maintains optimal performance under practical constraints, additional analyses are conducted to evaluate the stability of the proposed structures against typical fabrication tolerances. Figure 9 visualizes the comprehensive stability assessment through multi-parameter radar charts (for 10% tolerance) and detailed heat maps for: refractive index tolerance alone (a), unit cell layers' thickness tolerance alone (b), and joint index–thickness tolerance (c).

In consistence with the results presented above, all three photonic cavity structures (UIG-PMC, LIG-PMC, and PIG-PMC) demonstrate similar overall robustness changes versus the possible tolerances. These results also confirm that the effect of the tolerance in refractive index value of the layers is more that the case that we have the same amount of tolerances in the thickness values of the layers. Also as expected, the greatest drop in response will occur if tolerance is present in both the refractive index and the thickness of the layers.

Furthermore, a closer look at the considered metrics for evaluation of the response of the proposed structures shows that PPS remains perfectly stable with a constant value of 1 across all structures and tolerance levels (even at 10%), indicating it is completely unaffected by the imposed variations. On the other hand, in all cases of tolerance conditions and for all suggested cavities, SFI is consistently the most sensitive metric, decreases rapidly with increasing tolerance. Degradation in SFI value is even visible at low tolerance values of 1%. This sensitivity is most pronounced in the PIG-PMC structure, where SFI drops to even 0.4118 in case of 10% tolerance and joint index–thickness tolerance. The structures with central defect layer of having uniform and linear refractive indexes show similar SFI behavior, but the UIG-PMC structure just very slightly outperforms LIG-PMC at all tolerance levels, particularly at maximum 10%. The SCC metric show moderate degradation and is much more stable than SFI but less than PPS. In this case, the difference between structures is minor, both at low and high tolerances. All these results are also visible in the presented radar chart next to the heat maps. The plots reinforce that all three structures respond to large extent similarly to the tolerance changes. Also, the SFI metric demonstrates the highest sensitivity, showing the steepest decline and results in the asymmetrical profile which is more visible as tolerance increases.

As the last step, dependency of the spectral features robustness on the thickness of the central core layer inside the structures is also evaluated and the results are tabulated in Table 1 for two distinct tolerance values of 5% and 10%. As Fig. 4 shows, at thicker central layers, the differences between the proposed structures become more distinct. Thus, in this step, two thickness values of 3000 and 4000 nm were selected for analysis, both of which

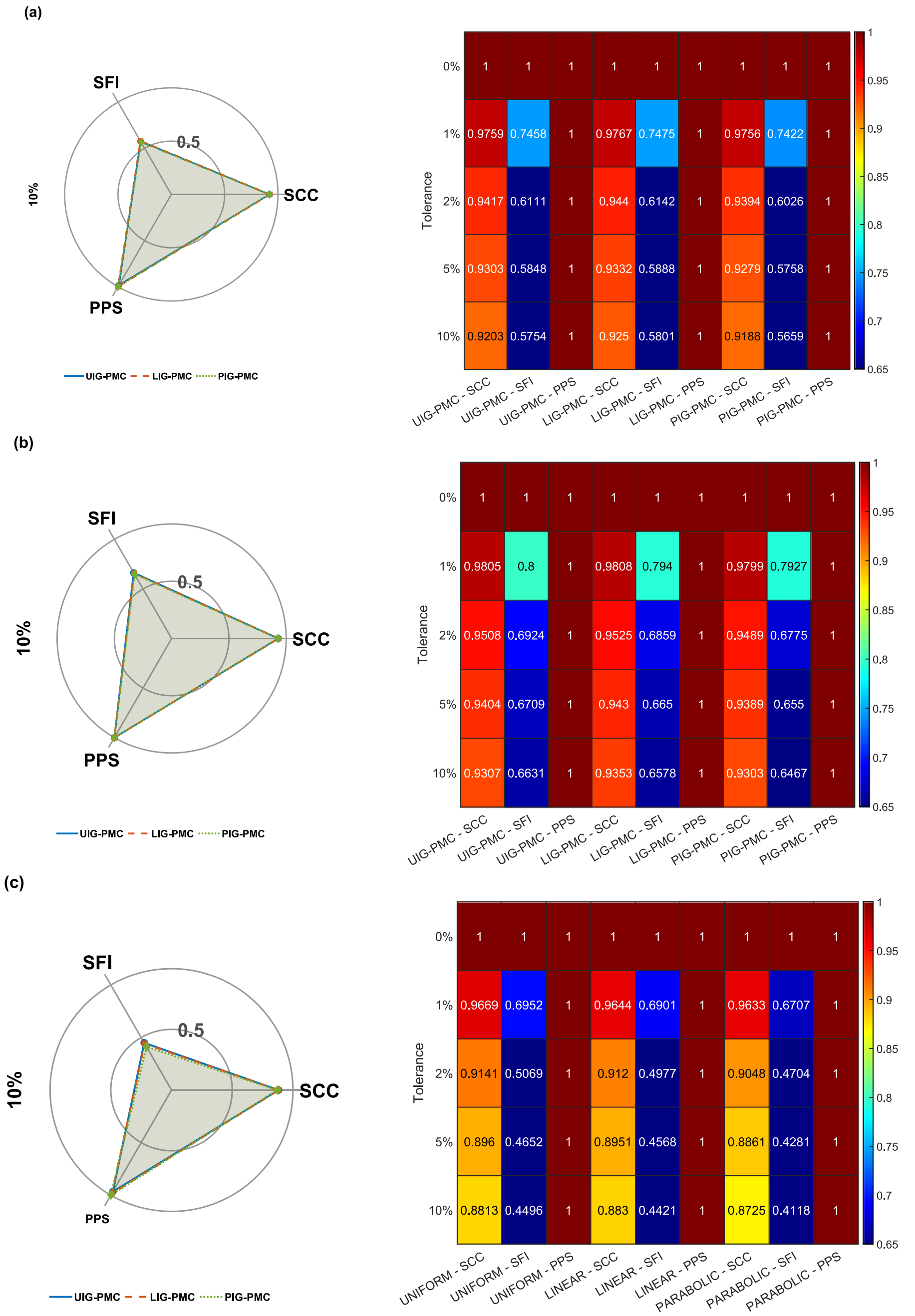

Fig. 9 Spectral robustness of the designed three photonic cavities under different tolerance conditions: **a** tolerance in refractive index only, **b** tolerance in TiO_2 and SiO_2 layer thickness only, and **c** tolerance in both parameters combined. Each panel includes radar charts for 10% tolerance level, with detailed heat maps. Other parameters are considered as explained in Fig. 4 and CCL thickness is 4 μm

Table 1 Spectral stability metrics at two tolerance values for the designed photonic cavity structures including different refractive index profiles at their central layer

Central core type	Tolerance of 5%						Tolerance of 10%					
	SCC		SFI		PPS		SCC		SFI		PPS	
	3000	4000	3000	4000	3000	4000	3000	4000	3000	4000	3000	4000
Uniform	0.903	0.896	0.469	0.465	1.00	1.00	0.889	0.881	0.454	0.450	1.00	1.00
Linear	0.896	0.895	0.457	0.457	1.00	1.00	0.883	0.883	0.442	0.442	1.00	1.00
Parabolic	0.884	0.886	0.431	0.428	1.00	1.00	0.871	0.873	0.415	0.412	1.00	1.00

Other parameters are considered as explained in Fig. 4

Table 2 Performance comparison of the proposed micro-cavities with other reported photonic crystal resonators

References No.	Structure features	Working wavelength	Studied parameters	Top Q-factor
Ours	1D-PC based UIG-PMC defect	400–750 nm $0<\theta<20$ degree	Q-factor: (+) Finesse: (+) Mode volume: (+) Statistical evaluation: (+)	$\sim 35\times 10^{3}$
Ours	1D-PC based LIG-PMC defect	400–750 nm $0<\theta<20$ degree	Q-factor: (+) Finesse: (+) Mode volume: (+) Statistical evaluation: (+)	$\sim 63\times 10^{3}$
Ours	1D-PC based PIG-PMC defect	400–750 nm $0<\theta<20$ degree	Q-factor: (+) Finesse: (+) Mode volume: (+) Statistical evaluation: (+)	$\sim 85\times 10^{3}$
Ben Ali (2017)	1D Fabry–Perot PC using hybrid Periodic, Fibonacci and Cantor photonic structures	440–540 nm $\theta<1.5$ Rad	Q-factor: (+) Finesse: (+) Mode volume: (–) Statistical evaluation: (–)	$\sim 3.1\times 10^{5}$
Bouazzi and Kanzari (2012)	1D Fabry–Perot PC based on hybrid Periodic/Rudin-Shapiro sequence	440–540 nm $\theta<1.5$ Rad	Q-factor: (+) Finesse: (+) Mode volume: (–) Statistical evaluation: (–)	$\sim 2.1\times 10^{5}$
Tavakoli and Jalili (2014)	1D-PC based on Simple Fibonacci structure	1.3–1.8 µm $\theta=0$	Q-factor: (+) Finesse: (–) Mode volume: (–) Statistical evaluation: (–)	$\sim 1\times 10^{4}$
Akahane et al. (2005)	2D-PC point-defect cavity	1.584–1.589 µm $\theta=0$	Q-factor: (+) Finesse: (–) Mode volume: (+) Statistical evaluation: (–)	$\sim 1\times 10^{5}$
Nakamura et al. (2016)	2D-L3 & H0 nanocavity PC	1.55 µm $\theta=0$	Q-factor: (+) Finesse: (–) Mode volume: (+) Statistical evaluation: (–)	1.7×10^{6}—5×10^{6}
Kassa-Baghdouchea et al. (2015)	2D-PC nanocavity (L3) SiN-based	680–740 nm $\theta=0$	Q-factor: (+) Finesse: (–) Mode volume: (+) Statistical evaluation: (–)	$\sim 2.5\times 10^{3}$
Xu et al. (2013)	Slotted 1D-PC with parabolic-width stack	1.565–1.595 µm $\theta=0$	Q-factor: (+) Finesse: (–) Mode volume: (+) Statistical evaluation: (–)	$\sim 10^{4}$
Mirsadeghi et al. (2013)	1D-PC slot micro-cavity based on silicon-on-insulator	~1.55 µm $\theta=0$	Q-factor: (+) Finesse: (–) Mode volume: (+) Statistical evaluation: (–)	$\sim 7.5\times 10^{3}$
Lu et al. (2021)	2D square PC and a 1D PC nanobeam cavity	540–700 nm $\theta=0$	Q-factor: (+) Finesse: (–) Mode volume: (+) Statistical evaluation: (–)	$\sim 1.16\times 10^{4}$

can be considered as good candidates for practical thickness selection. In overall, increasing the defect thickness from 3 to 4 µm does not change the PPS value and it remains the maximum value. Even though there are some exceptions but this increase in the thickness reduces very slightly the value of both SCC and SFI parameters at both considered tolerance values. This proves that the thickness increase (at least in this level) cannot worsen the robustness of the suggested structures to large extent. I.e. increasing CCL thickness does not amplify their sensitivity to fabrication errors. Furthermore, across both thicknesses and tolerance levels, the PIG-PMC structure maintains the lowest SFI and SCC values.

Finally, to provide a clearer overview, Table 2 compares the performance of the proposed microcavities with representative 1D/2D PC resonators reported in the literature. This table clearly reflects the advantages of our study in addition to the quality of performance of the suggested structures. While some optimized designs have demonstrated very large Q-factor values, it is worth highlighting some very important points here. These studies do not cover any statistical study by taking into consideration of the possible deviations from ideal conditions due to practical limitations during fabrication. Even though, our results are still much better than some of the already reported cases (Kassa-Baghdouchea et al. 2015; Tavakoli and Jalili 2014; Xu et al. 2013; Mirsadeghi et al. 2013; Lu et al. 2021) and fall within realistic experimental values (Tavakoli and Jalili 2014; Aurelio and Liscidini 2017; Yi and Li 2021). They additionally offer notable advantages as already discussed partly in sec.3.2 such as a simple one-dimensional design, including very limited unit cell numbers, wide incident angle operation range of 0 -20°, ease of fabrication using common dielectric materials, and robustness to dimensional tolerances of up to about 5%. Thus, we believe that these practical characteristics make the proposed design attractive for integrated photonic microresonator applications. To our knowledge, no experimental studies have investigated graded refractive index profiles in active PC micro-resonators in the visible range. Thus this theoretical study provides design guidelines and performance predictions that can guide future experimental implementations of such structures.

4 Conclusion

Polychromatic photonic micro-cavity resonator made of micro-meter sized fused silica core encapsulated between PC mirrors and cladding layers were suggested for high-precision wavelength control. Three cavity designs with uniform, linear, and parabolic refractive index profiles at central core were analysed using TMM routine. Q-factor, Finesse and mode volume calculations assessed spectral performance of the structures in detail and Monte Carlo simulations evaluated robustness through SCC, SFI, and PPS metrics under manufacturing tolerances. Results show that filling the cladding layer with active Rh6G instead of air does not increase the number of resonant modes but shifts the existing ones to longer wavelengths and increases their intensity. It was determined that 4–6 unit cells are sufficient to achieve the maximum number of active modes. Also, optimum performance for all proposed structures occurs within the 0–20° incident angle range. Adjusting the thickness of the unit cell building blocks can alter the optical response of the cavities, but the sensitivity to SiO_2 layer thickness is greater than to TiO_2. However, the dependency on the central core thickness is the most significant feature, and in all structures, increasing size of this layer to micrometer dimensions can dramatically enhance the number of resonant modes up to several tens of sharp peaks with acceptable Q-factor and finesse values.

The analysis revealed that regardless of the structure type, thickness, or tolerance level, PPS stays at maximum level of 1.00, indicating that peak positions are not significantly shifted, even under 10% tolerance in refractive index, thickness value or mixture of them. This means the spectral shape degrades, but resonance locations remain intact, an important trait for applications reliant on specific resonance positions. In general, both LIG-PMC and PIG-PMC with graded index profiles in their central core result in a much higher number of resonant peaks at their output compared to the cavity with a central core having a uniform refractive index. However it is worth noting that, even though just a few resonant modes in the LIG-PMC structure may have slightly lower Q-factors, but this configuration can be considered the optimal candidate according to SCC and SFI statistical evaluation of tolerance robustness assessments. But it doesn't mean that the performance differences between the LIG-PMC and PIG-PMC structures are large enough to rule out any of them for practical usage.

Thus, in summery it can be concluded that due to having simple configuration together with a tunable optical response while being strongly resilience to the possible tolerances during fabrication process, the suggested configurations (mostly LIG-PMC) may be useful in fulfillment of the wavelength selection needs in high precision micro-spectroscopy and optical communications applications.

Author contributions Conceptualisation: F. Ghasemi Theoretical modelling and statistical assessment: M. Khalili Hezarjaribi, S. Razi Supervision: F. Ghasemi Writing the manuscript draft: S. Razi, F. Ghasemi Final review and editing of the manuscript: F. Ghasemi, M. Khalili Hezarjaribi, S. Razi.

Data availability No datasets were generated or analysed during the current study.

Declarations

Competing Interests The authors declare no competing interests.

References

Akahane, Y., Asano, T., Song, B., Noda, S.: Fine-tuned high-Q photonic-crystal nanocavity. Opt. Express **13**, 1202 (2005). https://doi.org/10.1364/opex.13.001202

Alrowaili, Z.A., Medhat, M., Taha, T.A., Mehaney, A., Aljoufi, L.S., Elsayed, H.A.: One dimensional photonic crystal structure comprising a hyperbolic metamaterial for optical filtering purpose. Opt. Quant. Electron. **55**, 31 (2023)

Aurelio, D., Liscidini, M.: Electromagnetic field enhancement in Bloch surface waves. Phys. Rev. B **96**, 045308 (2017). https://doi.org/10.1103/PhysRevB.96.045308

Ben Ali, N.: Optical Fabry-Perot filters using hybrid periodic, Fibonacci and cantor photonic structures. Nano Commun. Netw. **13**, 34–42 (2017)

Bouazzi, Y., Kanzari, M.: Optical Fabry–Perot filter based on photonic band gap quasi-periodic one-dimensional multilayer according to the definite Rudin-Shapiro distribution. Opt. Commun. **285**, 2774–2779 (2012)

Cao, S., Chen, N., Jiang, Y.: Angle insensitive filters based on Fabry-Pérot resonance structures. J. Appl. Phys. **136**, 193102 (2024). https://doi.org/10.1063/5.0224213

Crowther, J.: Monochrome camera conversion: effect on sensitivity for multispectral imaging (ultraviolet, visible, and infrared). J. Imaging **8**(3), 54 (2022). https://doi.org/10.3390/jimaging8030054

de Jesús Acosta-Silva, Y., Toledano-Ayala, M., Gallardo-Hernández, S., Godínez, L.A., Méndez-López, A.: Investigation of TiO_2 deposit on SiO_2 films: synthesis, characterization, and efficiency for the photocatalytic discoloration of Methylene Blue in aqueous solution. Nanomaterials **13**(8), 1403 (2023). https://doi.org/10.3390/nano13081403

Fedoseev, V.N., Zhupanov, V.G.: Design of optical Fabry–Perot filters for spectral combination of laser beams. J. Opt. Technol. **88**, 683–687 (2021). https://doi.org/10.1364/JOT.88.000683

Ghasemi, F., Razi, S.: Novel photonic bio-chip sensor based on strained graphene sheets for blood cell sorting. Molecules **26**(18), 5585 (2021a)

Ghasemi, F., Razi, S.: Faraday rotator made of conjugated magneto active photonic crystal heterostructures. J. Magn. Magn. Mater. **538**, 168304 (2021b)

Ghasemi, F., Parvin, P., Lotfi, M.: Laser-induced fluorescence spectroscopy for diagnosis of cancerous tissue based on the fluorescence properties of formaldehyde. Laser Phys. Lett. **16**(3), 035601 (2019a)

Ghasemi, F., Roshan Entezar, S., Razi, S.: Graphene based photonic crystal optical filter: design and exploration of the tunability. Phys. Lett. A **383**, 2551–2560 (2019b)

Ghasemi, F., Aliasghary, M., Razi, S.: Magneto-sensitive photonic crystal optical filter with tunable response in 12–19 GHz. Cross over from design to prediction of performance using machine learning. Phys. Lett. A **401**, 127328 (2021)

Gua, nX., Liu, Q., Li, C., Yin, Z., Wu, J., Yu, P., Lu, W., Wang, S.: Generalized Fano resonance theory based on Fabry-Perot cavity. J. Phys. D Appl. Phys. **57**, 135102 (2024). https://doi.org/10.1088/1361-6463/ad1854

Hu, Y., Chen, H.: Eight-channel integrated device for electro-optic modulation and dense wavelength division multiplexing based on photonic crystals. Opt. Commun. **559**, 130407 (2024)

Hu, Z., Liao, X., Zhang, X., He, J.-J.: Widely tunable laser using reflecting Fabry-Perot filters with lossy half-wave trenches. IEEE Photonics J. **10**, 1–9 (2018). https://doi.org/10.1109/JPHOT.2017.2766878

Hua, J., Hua, E., Zhou, F., Shi, J., Wang, C., Duan, H., Hu, Y., Qiao, W., Chen, L.: Foveated glasses-free 3D display with ultrawide field of view via a large-scale 2D-metagrating complex. Light Sci. Appl. (2021). https://doi.org/10.1038/s41377-021-00651-1

Jahangiri, M., Parsanasab, G.-M., Moradiani, F.: Wavelength-selective single-mode laser by joint use of Parity-Time Symmetry and Vernier Effect in symmetric and asymmetric coupled microrings. J. Lightw. Technol. **42**, 1545–1555 (2024). https://doi.org/10.1109/JLT.2023.3324226

Kakiuchida, H., Sekiya, E.H., Shimodaira, N., Saito, K., Ikushima, A.J.: Refractive index and density changes in silica glass by halogen doping. J. Non-Cryst. Solids **353**, 568–572 (2007)

Kassa-Baghdouche, L., Cassan, E.: Sensitivity analysis of ring-shaped slotted photonic crystal waveguides for mid-infrared refractive index sensing. Opt. Quantum Electron. **51**, 328 (2019). https://doi.org/10.1007/s11082-019-2040-4

Kassa-Baghdouchea, L., Boumaza, T., Cassan, E., Bouchemat, M.: Enhancement of Q-factor in SiN-based planar photonic crystal L3nanocavity for integrated photonics in the visible-wavelength range. Optik **126**, 3467–3471 (2015). https://doi.org/10.1016/j.ijleo.2015.07.150

Kim, B., Ahn, J., Jeong, J., Jeo, nY., Jeon, K., Hwang, K.: Preparation of TiO_2 thin film on SiO_2 glass by a spin coating–pyrolysis process. Ceram. Int. **32**, 223–225 (2006)

Kim, H., Song, B., Asano, T., Noda, S.: High-Q silicon two-dimensional photonic crystal slot nanocavities with asymmetric low-index claddings. Appl. Phys. Lett. **126**, 051101 (2025). https://doi.org/10.1063/5.0233913

Li, W.T., Bulla, D.A.P., Charles, C., Boswell, R., Love, J., Luther-Davies, B.: Ge-doped SiO_2 thin films produced by helicon activated reactive evaporation. Thin Solid Films **419**, 82–87 (2002). https://doi.org/10.1016/S0040-609(02)00711-3

Liu, L., Long, Y.: Machine-learning-powered efficient design of photonic crystal cavities. PhotoniX **6**, 37 (2025). https://doi.org/10.1186/s43074-025-00201-7

Lu, T.W., Feng, Y.K., Chu, H.Y., Lee, P.T.: Photonic crystal polymeric thin-film dye-lasers for attachable strain sensors. Sensors **21**, 5331 (2021). https://doi.org/10.3390/s21165331

Mirsadeghi, S.H., Schelew, E., Young, J.F.: Photonic crystal slot-microcavity circuit implemented in silicon-on-insulator: high Q operation in solvent without undercutting. Appl. Phys. Lett. **102**, 131115 (2013). https://doi.org/10.1063/1.4799963

Mitra, M., Haworth, A., Gaddale, P., Badran, F., Lagno, N., Pameijer, C., Aziz, F., Kothapalli, S.: Multi-wavelength laser diode based portable photoacoustic and ultrasound imaging system for point of care applications. J. Biophotonics **17**(7), e202400058 (2024). https://doi.org/10.1002/jbio.202400058

Muhammad, S., Chen, D., Xian, C., Zhou, J., Lei, Z., Kuang, P., Li, Z., Wen, G., Huang, Y.: Design and fabrication of high-quality two-dimensional silicon-based photonic crystal optical cavity with integrated waveguides. Photonics **11**(8), 753 (2024). https://doi.org/10.3390/photonics11080753

Nakamura, T., Takahashi, Y., Tanaka, Y., Asano, T., Noda, S.: Improvement in the quality factors for photonic crystal nanocavities via visualization of the leaky components. Opt. Express **24**, 9541 (2016). https://doi.org/10.1364/OE.24.009541

Plock, M., Binkowski, F., Zschiedrich, L., Schneider, P., Burger, S.: Fabrication uncertainty guided design optimization of a photonic crystal cavity by using Gaussian processes. J. Opt. Soc. Am. B **41**(4), 850 (2024). https://doi.org/10.1364/JOSAB.505767

Qi, D., Wang, X., Cheng, Y., Chen, F., Liu, L., Gong, R.: Quasi-periodic photonic crystal Fabry-Perot optical filter based on Si/SiO_2 for visible-laser spectral selectivity. J. Phys. D Appl. Phys. **51**, 225103 (2018)

Razi, S., Ghasemi, F.: Broad band temperature independent photonic crystal based optical filter with response in visible wavelength range. Laser Phys. **29**(4), 046204 (2019a)

Razi, S., Ghasemi, F.: One-dimensional structure made of periodic slabs of SiO_2/InSb offering tunable wide band gap at terahertz frequency range. Chin. Phys. B **28**, 124205 (2019b)

Razi, S., Mollabashi, M., Madanipour, K.: Nanosecond laser surface patterning of bio grade 316L stainless steel for controlling its wettability characteristics. Int. J. Opt. Photonics **9**(1), 43–57 (2015)

Roshan Entezar, S., Ghasemi, F., Razi, S.: Tunable resonant Bragg photonic bandgap structures based on active quantum dot layers; crystals with applications in all-optical switches manufacturing. Waves Random Complex Media **32**(2), 676–695 (2022)

Segovia-Chaves, F., Vinck-Posada, H.: Dependence of the defect mode with temperature, pressure and angle of incidence in a 1D semiconductor-superconductor photonic crystal. Phys. C Supercond. Appl. **553**, 1–7 (2018). https://doi.org/10.1016/j.physc.2018.07.001

Sepahvandi, V., Rezaei, B., Aly, A.H.: Tunable multichannel Fibonacci one-dimensional terahertz photonic crystal filter. Sci. Rep. **13**, 5631 (2023)

Serna, S., Colman, P., Zhang, W., Le Roux, X., Caer, C., Vivien, L., Cassan, E.: Experimental GVD engineering in slow light slot photonic crystal waveguides. Sci. Rep. **6**, 26956 (2016). https://doi.org/10.1038/srep26956

Tavakoli, M., Jalili, Y.S.: One-dimensional Fibonacci fractal photonic crystals and their optical characteristics. J. Theor. Appl. Phys. **8**, 1–12 (2014)

Wafa, M.I., El-Batawy, Y.M., El-Naggar, S.A.: Stochastic modeling of 2D photonic crystals. Opt. Quantum Electron. (2021). https://doi.org/10.1007/s11082-021-02914-y

Wang, Z., Wang, J., Xu, H., Wen, Q., Li, D., Li, J.: High-precision electromagnetic tuning of Fabry-Pérot filters for gas detection. IEEE Sens. J. **25**, 6425–6432 (2025). https://doi.org/10.1109/JSEN.2024.3518476

Wu, F., She, Y., Cheng, Z., Hu, S., Liu, G., Xiao, S.: Anomalous polarization-sensitive Fabry-Perot resonance in a one-dimensional photonic crystal containing an all-dielectric metamaterial defect. Opt. Express **31**, 32669–32683 (2023). https://doi.org/10.1364/OE.499830

Wu, X., Lin, Z., Tang, S., Chen, X., Guo, T., He, S.: A multi-resonant tunable Fabry-Pérot cavity for high throughput spectral imaging. Adv. Opt. Mater. **13**, 2402784 (2025). https://doi.org/10.1002/adom.202402784

Xu, P., Yao, K., Zheng, J., Guan, X., Shi, Y.: Slotted photonic crystal nanobeam cavity with parabolic modulated width stack for refractive index sensing. Opt. Express **21**, 26908–26913 (2013). https://doi.org/10.1364/OE.21.026908

Xu, B., Zheng, G., Wu, Y., Cao, K.: Transmission properties of defect modes in one-dimensional photonic crystals containing gradient refractive index defects. Optik **126**(24), 5158–5162 (2015)

Yi, L., Li, C.: Simulation research on blood detection sensing with parity-time symmetry structure. Crystals **11**, 1030 (2021). https://doi.org/10.3390/cryst11091030

Yu, H., Liu, X., Sun, W., Xu, Y., Liu, X., Liu, Y.: A brief review of whispering gallery mode in sensing. Opt. Laser Technol. **177**, 111099 (2024)

Yuan, Y., Zhang, Y., Zhang, H., Xiang, G., Zhang, Z., Xiong, L.: Narrow-band filter of Fabry-Pérot cavity over a wide spectrum range based on second-order resonant peak. Opt. Express **33**, 28081–28096 (2025). https://doi.org/10.1364/OE.565067

Zaky, Z.A., Alamri, S., Zhaketov, V.D., Aly, A.H.: Refractive index sensor with magnified resonant signal. Sci. Rep. **12**, 13777 (2022). https://doi.org/10.1038/s41598-022-17676-0

Zhou, L., Wang, B., Zhang, W.: On-chip reconfigurable high-order Fabry-Perot filter using fully tunable Sagnac loop mirrors. J. Lightwave Technol. **43**, 7293–7304 (2025). https://doi.org/10.1109/JLT.2025.3574736